van der Veen CJ and Whillans IM (1989) Force Budget: I. Theory and Numerical Methods. *Journal of Glaciology*, **35**(119), 53–60, ISSN 0022-1430 (doi: 10.3189/002214389793701581)

Vijay S, King MD, Howat IM, Solgaard AM, Khan SA and Noël B (2021) Greenland ice-sheet wide glacier classification based on two distinct seasonal ice velocity behaviors. *Journal of Glaciology*, **67**(266), 1241–1248, ISSN 0022-1430 (doi: 10.1017/JOG.2021.89)

Wang W, Li J and Zwally HJ (2012) Dynamic inland propagation of thinning due to ice loss at the margins of the Greenland ice sheet. *Journal of Glaciology*, **58**(210), 734–740, ISSN 00221430 (doi: 10.3189/2012JoG11J187)

Weertman J (1957) On the Sliding of Glaciers. *Journal of Glaciology*, **3**(21), 33–38, ISSN 0022-1430 (doi: 10.3189/S0022143000024709)

Wood M, Rignot E, Fenty I, An L, Bjørk A, van den Broeke M, Cai C, Kane E, Menemenlis D, Millan R, Morlighem M, Mouginot J, Noël B, Scheuchl B, Velicogna I, Willis JK and Zhang H (2021) Ocean forcing drives glacier retreat in Greenland. *Science Advances*, **7**(1), 1–11, ISSN 23752548 (doi: 10.1126/sciadv.aba7282)

Zheng W (2022) Glacier geometry and flow speed determine how Arctic marine-terminating glaciers respond to lubricated beds. *Cryosphere*, **16**(4), 1431–1445, ISSN 19940424 (doi: 10.5194/TC-16-1431-2022)

A APPENDIX A: SUPPLEMENTARY TABLES

Synthetic testbeds geometry at steady state					
Name	Width (m)	Depth (effective depth) (m)	Floating termini length (km)	Surface slope	Boundary influx (m^3s^{-1})
W1GL0FC1	4000	-100 (-142)	0	0.020	86.13
W1GL1FC1	4000	-500 (-474)	4.72	0.013	109.87
W1GL0FC2	4000	-100 (-142)	0	0.026	46.45
W1GL1FC2	4000	-500 (-487)	3.99	0.016	55.26
W1GL0FC3	4000	-100 (-139)	0	0.035	28.13
W1GL1FC3	4000	-500 (-488)	4.16	0.023	32.94
W2GL0FC1	6000	-100 (-157)	0	0.015	130.65
W2GL1FC1	6000	-500 (-458)	8.45	0.012	172.73
W2GL0FC2	6000	-100 (-158)	0	0.020	59.32
W2GL1FC2	6000	-500 (-464)	7.88	0.014	71.19
W2GL0FC3	6000	-100 (-156)	0	0.028	33.62
W2GL1FC3	6000	-500 (-467)	7.75	0.020	37.21
W3GL0FC1	8000	-100 (-162)	0	0.013	169.70
W3GL1FC1	8000	-500 (-425)	11.54	0.013	223.70
W3GL0FC2	8000	-100 (-164)	0	0.017	68.54
W3GL1FC2	8000	-500 (-426)	11.42	0.014	81.53
W3GL0FC3	8000	-100 (-162)	0	0.024	37.021
W3GL1FC3	8000	-500 (-428)	11.26	0.021	40.99

Table A1. Characteristics of the synthetic testbeds at their steady state. The nomenclature of the testbed names: "W" stands for fjord width, "GL" stands for grounding line depth, and "FC" stands for the sliding law coefficient. Numbers that follow: 1 to 3 represent low to high values; 0 and 1 respectively represent the testbed glaciers with shallow and deep grounding lines. "Depth" is the grounding line depth at the start of the model relaxation, and "effective depth" means grounding line depth after the model relaxation. "Surface slope" averages the slopes at the first 10 km behind the grounding line. "Boundary influx" is the total flux into the model domain across the width.

Kinematic characteristics of synthetic testbeds at steady state									
Name	Velocity (m a^{-1})			Thickness (m)			Basal drag (kPa)		
	min	mean	max	min	mean	max	min	mean	max
W1GL0FC1	2585	3470	4898	111	303	389	16	27	57
W1GL1FC1	1530	2168	2333	342	545	572	8	18	42
W1GL0FC2	1164	1684	2702	117	340	451	35	49	84
W1GL1FC2	814	1087	1246	327	555	599	16	33	63
W1GL0FC3	571	865	1619	125	402	544	82	94	127
W1GL1FC3	526	653	806	302	554	633	41	74	101
W2GL0FC1	2448	3306	4162	131	279	331	13	23	30
W2GL1FC1	1478	2184	2357	294	503	519	8	15	25
W2GL0FC2	1050	1418	1963	133	303	374	25	38	45
W2GL1FC2	674	942	1096	272	496	528	14	26	38
W2GL0FC3	481	689	1098	138	356	458	51	73	85
W2GL1FC3	399	521	650	241	476	542	33	57	71
W3GL0FC1	2102	3131	3765	134	265	306	10	21	26
W3GL1FC1	1352	2180	2349	253	461	480	7	15	21
W3GL0FC2	872	1228	1588	133	281	337	17	33	39
W3GL1FC2	568	867	1004	224	437	479	11	24	31
W3GL0FC3	416	575	844	135	326	412	36	61	68
W3GL1FC3	332	485	587	194	398	471	26	52	65

Table A2. Kinematic characteristics of the synthetic testbeds at their steady state. Testbed nomenclature is the same as in Table A1. The statistics of velocity, thickness, and basal drag are calculated based on the data from the first 10 km behind the grounding line.

Maximum ΔH and dH/dt in the localized basal perturbation experiment				
	Diffused pulse		Transient pulse	
Name	max ΔH(m)	max dH/dt (m a^{-1})	max ΔH(m)	max dH/dt (m a^{-1})
W1GL0FC1	4.87	4.91	3.63	21.81
W1GL1FC1	7.48	6.79	5.93	30.81
W1GL0FC2	5.31	5.38	3.67	20.34
W1GL1FC2	9.35	9.06	7.58	41.39
W1GL0FC3	5.58	5.02	3.47	18.46
W1GL1FC3	10.76	10.57	8.56	45.88
W2GL0FC1	5.69	5.48	3.86	22.08
W2GL1FC1	9.29	8.48	6.78	32.32
W2GL0FC2	5.82	5.24	3.56	18.67
W2GL1FC2	9.91	9.89	7.73	40.16
W2GL0FC3	5.88	4.44	3.26	15.78
W2GL1FC3	10.73	10.48	8.05	41.86
W3GL0FC1	6.29	5.93	4.05	22.59
W3GL1FC1	10.29	11.24	7.00	32.43
W3GL0FC2	5.98	4.93	3.44	17.39
W3GL1FC2	7.91	8.60	5.89	31.61
W3GL0FC3	5.86	3.96	3.10	13.49
W3GL1FC3	8.68	8.17	6.11	32.44

Table A3. Maximum absolute elevation change and change rate in localized basal perturbation experiments. Testbed nomenclature is the same as shown in table A1.

Max thinning rate (m a^{-1})		Shallow testbeds			Deep testbeds		
		Mean basal shear stress					
		Low	Medium	High	Low	Medium	High
Fjord width	Narrow	5.0	5.5	6.2	10.4	12.0	16.0
	Medium	4.1	4.5	5.3	10.4	10.1	12.5
	Wide	3.7	4.0	4.7	10.5	8.4	9.4

Table A4. Max thinning rate from overburden pressure experiment, accompanying Fig. 3

Attenuation distance (km)		Shallow testbeds			Deep testbeds		
		Mean basal shear stress					
		Low	Medium	High	Low	Medium	High
Fjord width	Narrow	31.0	25.3	19.8	32.8	28.2	22.7
	Medium	30.6	24.5	19.3	33.6	28.9	23.8
	Wide	30.4	23.8	18.7	33.8	29.0	24.4

Table A5. Attenuation distance of diffusive thinning from overburden pressure experiment.

B APPENDIX B: SUPPLEMENTARY METHOD

B.1 Ice dynamics simulation

We use the MATLAB version of Ice-sheet and Sea-level System Model (ISSM version 4.21) to simulate ice flow dynamics. In the following sections, the definitions of variables can be found in Table 1 in the main text.

B.2 Synthetic testbed

For all testbeds, we applied a linear surface mass balance relationship:

$$\mathrm{SMB}(x) = 0.5(1 - \frac{2}{L_x}x) \tag{B.4}$$

where x is the distance from the influx boundary and L_x is the along-flow domain length. This fixes the equilibrium line altitude at $x = L_x/2$.

The across-flow bed topography was prescribed similarly to Felikson and others (2022)

$$B_y(y) = \frac{d_c}{1 + e^{-2/f_c(y - L_y/2 - w_c(x))}} + \frac{d_c}{1 + e^{-2/f_c(y - L_y/2 + w_c(x))}} \tag{B.5}$$

where y is across-flow direction, L_y is model domain width, f_c is the characteristic width of channel side walls, and d_c defines the depth of the trough compared to the top of side walls.

In our base experiments, we did not allow bed topography undulation for our base experiments and therefore prescribed the along-flow bedrock depth as a linear function:

$$B_x(x) = B_0 + \left(\frac{B_{gl} - B_0}{L_x}\right)x \tag{B.6}$$

where B_0 is the bed depth at the influx boundary and B_{gl} is the grounding line depth, and the bed slopes toward the ocean (prograde) to mitigate any potential run-away retreat. In the upper reaches of the glacier, the width of the trough $w_c(x)$ narrows along the flow. It has a funnel shape that starts with a fixed width (across all testbeds) at the inflow boundary and narrows for the first $x_f = 15$ km and reaches a constant width (variable across testbeds) throughout the rest of the flow trunk, which is the majority of the model domain. We designed this shape to accommodate our requirement that each testbed glacier receives the same ice influx at the domain top during initialization, regardless of glacier width at the terminus. We parameterized the narrowing stage with a parabolic function:

$$w_c(x) = \begin{cases} \left[\left(\frac{L_y/W-1}{{x_f}^2}\right)(x - x_f)^2 + 1\right]W & 0 \leqslant x \leqslant x_f \\ W & x > x_f \end{cases} \tag{B.7}$$

The prescribed Weertman sliding law coefficient C_w for model initialization is spatially variable. Its lateral variability is prescribed to be similar to the bed topography while its along-flow variation is conditioned to decay exponentially toward the calving front:

$$C_w(x,y) = \frac{C_{w0}(3-e)e^{-2(x/L_x)}}{1 + e^{-2/f_c(y - L_y/2 - w_c(x))}} + \frac{C_{w0}(3-e)e^{-2(x/L_x)}}{1 + e^{2/f_c(y - L_y/2 + w_c(x))}} \tag{B.8}$$

The numerator helps define the e-folding length over which the sliding law coefficient decreases toward the terminus. This serves to regulate the ice velocity near the influx boundary and alleviate solver convergence issues when the prescribed sliding law coefficient law is low.

To initialize the model, we used the plastic ice sheet profile as an initial guess of glacier thickness, assuming an ice plastic yield strength of 1 MPa:

$$H(x) = \sqrt{\frac{2\tau_0(L-x)}{\rho_i g}} \tag{B.9}$$

where τ_0 is the ice plastic yield strength, L the glacier length, ρ_i the ice density, and g the gravitational constant. Since all testbed glaciers have the same length from the ice front to the influx boundary, they have identical initial ice thickness, and it is fixed as a Dirichlet boundary condition there. Similarly, we fixed the influx velocity at 100 km a^{-1} at the influx boundary, thus keeping the influx constant across all glaciers before model relaxation.

During the initialization, the transient simulations have an adaptive time step based on the Courant–Friedrichs–Lewy condition. During subsequent "control" and "overburden pressure experiment" runs, the time steps are fixed at 0.1 year. During the localized basal perturbation runs, the time steps are fixed at 0.01 year, although we only record the simulation output every 0.1 year.

B.3 Experiment design

B.3.1 Control

After the testbed was initialized to its steady state, we forced the calving front to retreat at a rate characterized by a triangular function:

$$\nu(t) = \begin{cases} \frac{\nu_m t_s}{t_s - t_e} + \frac{\nu_m}{t_e - t_s} t & t_s < t \leqslant (t_s + t_e)/2 \\ \frac{\nu_m t_e}{t_e - t_s} - \frac{\nu_m}{t_e - t_s} t & (t_s + t_e)/2 < t \leqslant t_e \\ 0 & \text{otherwise} \end{cases} \tag{B.10}$$

where we defined ν_m as the maximum retreat rate, and t_s and t_e the start and end year of calving front perturbation.

B.3.2 Overburden pressure experiment

Here we provide a more detailed derivation of Eq.3. Noted that in Weertman's law (Eq.1), the sliding law coefficient C_w is raised to $1/m$, but in ice-sheet modeling such as ISSM, the coefficient is generally acquired through inversion to achieve momentum equilibrium and does not require to possess a physical meaning. Therefore in ISSM, Weertman's law coefficient is simply a non-zero fitting coefficient and thus the law is implemented as

$$\boldsymbol{\tau}_b = C_w^2 ||\mathbf{v}_b||^{1/m-1} v_b \tag{B.11}$$

Notice that it is C_w^2, not $C_w^{1/m}$ in Eq.1. To derive Eq.3 we used the formulation above. First, since the model is initialized and relaxed with Weertman's law, to emulate Budd's sliding and investigate the effect of ice overburden stress, we can write an equivalent Budd's sliding law coefficient $\hat{C}_b$ by equating the two sliding laws (assuming q = 1) i.e. $C_w^2||\mathbf{v}_b||^{1/m-1}v_b = C_b^2 N^{1/m}||\mathbf{v}_b||^{1/m-1}v_b$. Therefore the equivalent Budd's sliding law coefficient $\hat{C}_b$ is

$$\hat{C}_b = \frac{C_{w0}}{[\rho_i g H(t=0)]^{1/2m}} \tag{B.12}$$

At any time t, we require that the change in Weertman's sliding law coefficient $C_w(t)$ match the change in the effective pressure N. The change in Weertman's sliding law coefficient between a time t and 0 is $C_w^2(t) - C_{w0}^2$ and the change in Budd's sliding law prefactor (which includes the coefficient and the effective pressure N) is $\hat{C}_b^2 N^{1/m}(t) - \hat{C}_b^2 N^{1/m}(t=0)$. Again, the effective pressure is defined as $N = \rho_i g H - p_w$. Equating them gives us:

$$C_w^2(t) - C_{w0}^2 = \hat{C}_b^2 N^{1/m}(t) - \hat{C}_b^2 N^{1/m}(t=0) \tag{B.13}$$

$$C_w^2(t) = C_{w0}^2 + \hat{C}_b^2[N^{1/m}(t) - N^{1/m}(0)] \tag{B.14}$$

$$C_w^2(t) = C_{w0}^2 + \hat{C}_b^2[(\rho_i g H(t) - p_w)^{1/m} - (\rho_i g H(0) - p_w)^{1/m}] \tag{B.15}$$

$$C_w(t) = \sqrt{C_{w0}^2 + \hat{C}_b^2[(\rho_i g H(t) - p_w)^{1/m} - (\rho_i g H(0) - p_w)^{1/m}]} \tag{B.16}$$

Eq.3 is derived.

B.3.3 Localized basal perturbation

While the overburden pressure experiment accounts for changes in ice overburden pressure from ice thickness change, a localized reduction of basal drag represents basal lubrication due to meltwater. Mathematically, we wrote the sliding law coefficients as

$$C_{bp} = C_b + \Delta C(x, y, t; \hat{w}) \tag{B.17}$$

where C_{bp} is the sliding law coefficient for localized basal perturbation, C_b the sliding law coefficient for overburden pressure experiment (Budd sliding), and $\Delta C(x, y, t; w)$ is determined by either of the two pulses:

$$\Delta C(x,y,t;\hat{w})_{\mathrm{TP}} = \hat{C}\exp\left[-3\left(\frac{t}{t_p}\right)^2\right]\exp\left[-\frac{(x-x_0)^2}{2\hat{w}^2}-\frac{(y-W/2)^2}{2\hat{w}^2}\right] \tag{B.18}$$

$$\Delta C(x,y,t;\hat{w})_{\mathrm{DP}} = \hat{C}\left(\frac{t_p}{t_d}\right)\exp\left[-3\left(\frac{t}{t_d}\right)^2\right]\exp\left[-\frac{(x-x_0)^2}{2\hat{w}^2}-\frac{(y-W/2)^2}{2\hat{w}^2}\right] \tag{B.19}$$

Here t_p and t_d are respectively the characteristic timescale of Transient Pulse and Diffused Pulse, and $\hat{C}$ and $\hat{w}$ are scaled sliding law coefficient and localized basal perturbation patch width (one standard deviation), defined as

$$\hat{C} = \phi C_w \tag{B.20}$$

$$\hat{w} = \kappa W\sqrt{\frac{W}{\max(\mathrm{W})}} \tag{B.21}$$

where max(W) is the largest fjord width we construct, and κ is the ratio of Gaussian basal perturbation width to fjord width, here set to 0.08. In other words, $\hat{C}$ denotes a proportional reduction of sliding law coefficient at the initial state defined in equation B.8, $\hat{w}$ denotes a quadratic scaling relation between the fjord width and the perturbation patch width, which is a consequence of the requirement that the fractional area being perturbed in each glacier remains identical across the testbeds, i.e., $\left(\int \Delta C(x,y;W_1)\,dx\,dy\right)/\left(\int_A dx\,dy\right) = \left(\int \Delta C(x,y;W_2)\,dx\,dy\right)/\left(\int_A dx\,dy\right)$ in which W_1 and W_2 represent two different fjord widths, and A is an arbitrarily chosen flow area that fully encloses the perturbation.

We formulate the parameterization ensuring that total changes in the two sliding law coefficient are the same in each perturbation cycle: $\int \Delta C_{\mathrm{TP}}(t)dt = \int \Delta C_{\mathrm{DP}}(t)dt$, as stated in the method section. At the end of each perturbation cycle, the perturbation in the sliding law coefficient ΔC returns to near-zero level ($\Delta C < 10^{-4}$ kg m^{-2} s^{-1}). Moreover, we previously mentioned that we scaled the magnitude of the sliding law coefficient reduction linearly with respect to the coefficient at the initial state, denoted by ϕC_w. This decision was made due to a lack of knowledge regarding any general relationship between basal lubrication and various hydrological and glacier geometric factors.

It should be noted that since ΔC_{TP} and ΔC_{DP} depend on the initial sliding law coefficient C_w, combining the reductions in the sliding law coefficient from both localized basal perturbation and overburden pressure may result in C_{bp} dropping below zero as the simulation progresses. In such a case, we force the local sliding law coefficient to a minimum of 0 until it rebounds as the localized basal perturbation recovers.

B.4 Stress balance

The stress balance states that the gravitational driving stress of a glacier is approximately in balance with the sum of the basal shear stress and the longitudinal and lateral resistive stress gradients:

$$\tau_d \approx \tau_b + \frac{\partial}{\partial x}\left(HR_{xx}\right) + \frac{\partial}{\partial y}\left(HR_{xy}\right) \tag{B.22}$$

The longitudinal resistive stress R_{xx} and the lateral resistive stress R_{xy} can be calculated respectively as

$$R_{xx} = B\ \dot{\epsilon}_e^{1/n-1}(2\dot{\epsilon}_{xx} + \dot{\epsilon}_{yy}) \tag{B.23}$$

$$R_{xy} = B\ \dot{\epsilon}_e^{1/n-1}\dot{\epsilon}_{xy} \tag{B.24}$$

where B is ice rigidity; $\dot{\epsilon}_{xx}$, $\dot{\epsilon}_{xy}$, and $\dot{\epsilon}_{yy}$ are strain rates in the subscripted directions, and $\dot{\epsilon}_e$ is the effective strain rate, defined here as its second tensor invariant, as is commonly done:

$$\dot{\epsilon}_e = (\dot{\epsilon}_{xx}^2 + \dot{\epsilon}_{xy}^2 + \dot{\epsilon}_{yy}^2 + \dot{\epsilon}_{xx}\dot{\epsilon}_{yy})^{1/2} \tag{B.25}$$

We applied a five-point finite difference stencil to calculate spatial derivatives and then smoothed the derived stress components using a Gaussian filter with a 2 km standard deviation, which we chose to be approximately 5–7 times the ice thickness, following Frank and others (2022). The smoothing has a dual purpose: to reduce noise resulting from computing the numerical derivative and to account for the coupling length of the longitudinal stress gradient (Kamb and Echelmeyer, 1986; Enderlin and others, 2016).

To calculate the frontal resistive stress loss ΔR (Sect. 2.5), we differenced the frontal resistive stress summed along the glacier from the calving front to the grounding line, between the first and last time steps:

$$\Delta R = \int_0^{t_e} \frac{d}{dt}\left[\int_{X_g(t)}^{X_c(t)} \left(\tau_b + \frac{\partial}{\partial x}(HR_{xx}) + \frac{\partial}{\partial y}(HR_{xy})\right) dx\right] dt \tag{B.26}$$

where X_g denotes the location of the grounding line, X_c the location of the calving front, and t_e the final year of the perturbation. We evaluate the integral numerically with the trapezoidal rule.

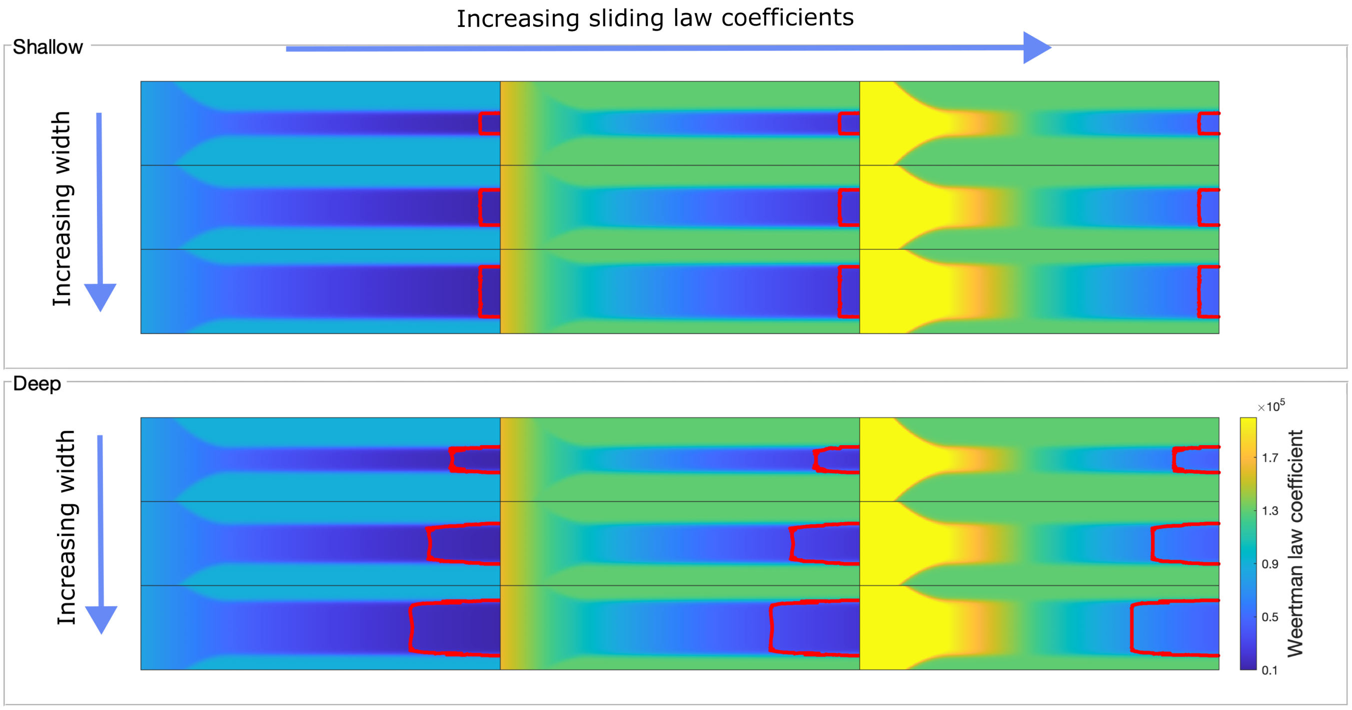

Fig. A1. The Weertman's sliding law coefficients (Eq.B.8) for all 18 testbed glaciers to initialize the models. Red lines mark the grounding line positions at the steady state. Models with shallow and deep grounding lines are grouped separately; each group is arranged along two directions: increasing fjord width and increasing sliding law coefficients.

789 # C APPENDIX C: SUPPLEMENTARY FIGURES

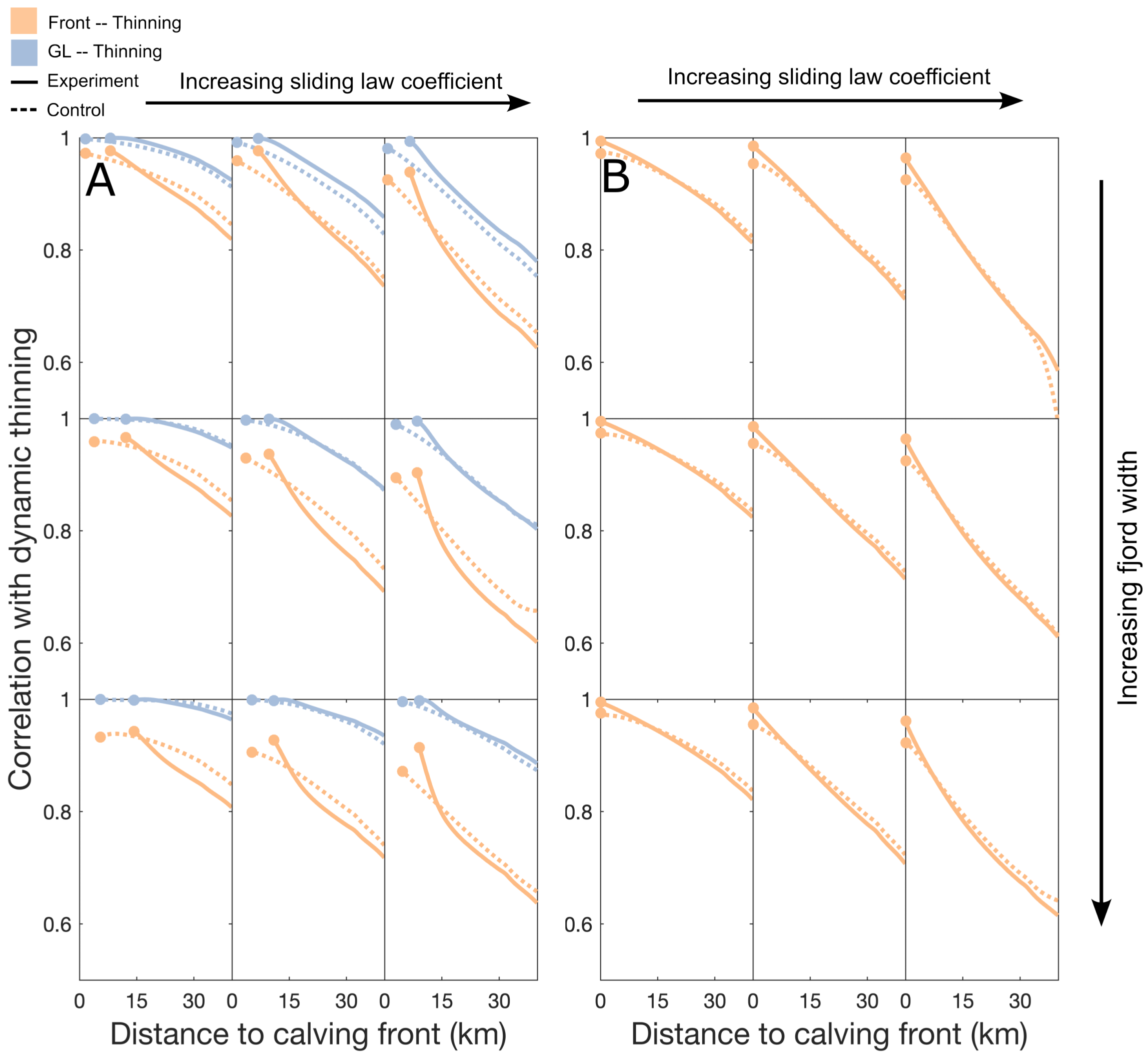

Fig. A2. Timeseries correlation over the 16-year perturbation between dynamic thinning and the grounding line position (blue), and dynamic thinning and frontal retreat (orange). The correlation is measured by Pearson correlation coefficient and we used `corrcoef` function in MATLAB for the calculation. For a given model run, thinning rates are sampled at every 0.1 year at every 100 meters along the central flowline, plotted here along the x-axis. "GL" denotes grounding line retreat. "Experiment" represents the overburden pressure experiment and "Control" represents the control run. Round markers represent the last position of either the ice front or the grounding line. A) Results for deep testbed glaciers. B) Results for shallow testbed glaciers. No correlations between grounding line and thinning are shown because all glaciers remain fully grounded throughout the simulations, and hence no grounding line is defined.

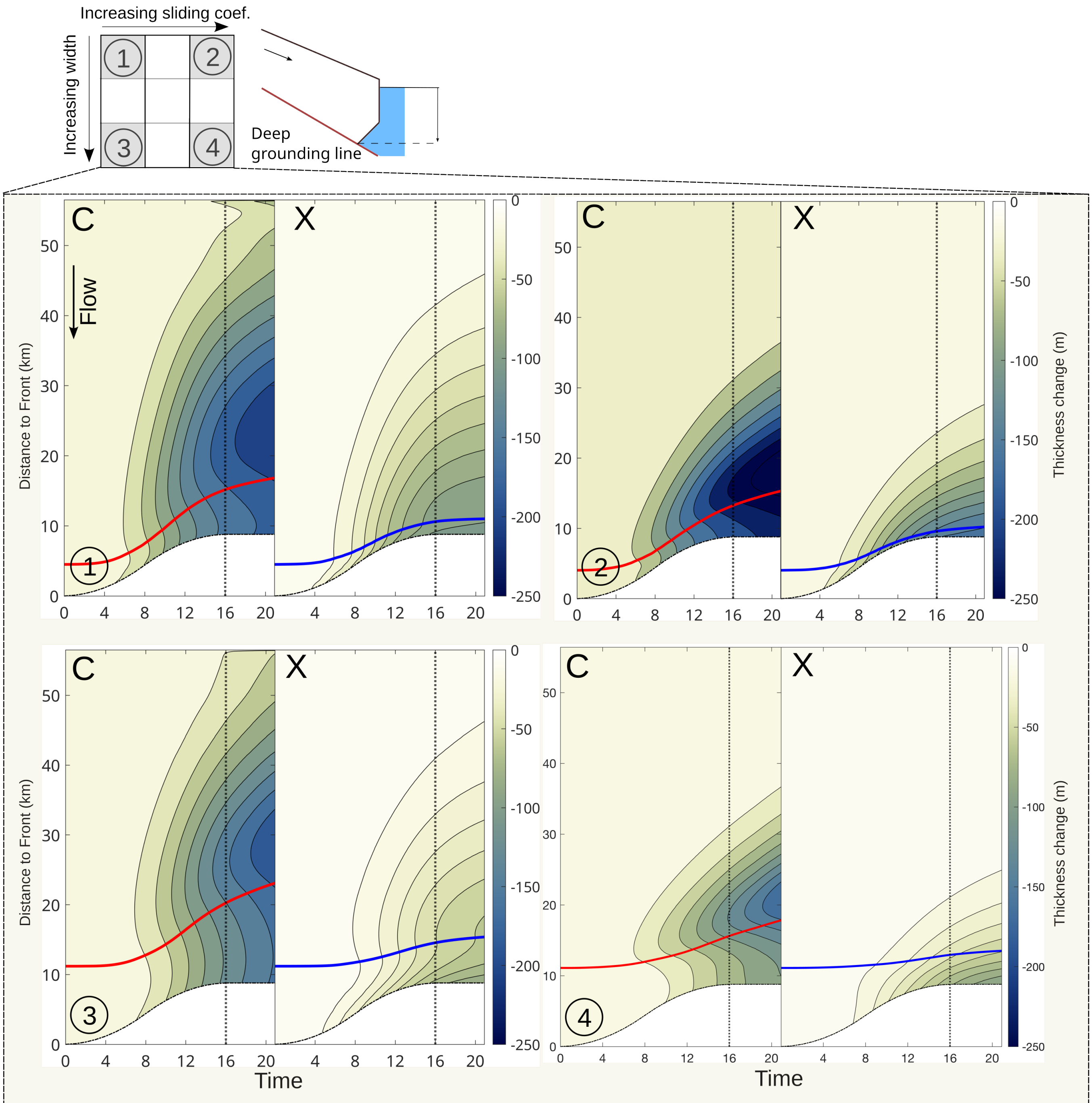

Fig. A3. Dynamic thickness change in **deep** testbed glaciers along the center flow line over time, using $m = 5$ in Budd sliding law, in comparison to $m = 1$ in the main text (Figure 3). Different from the main text, here we are comparing two simulations both using Budd's law but different exponents m on the sliding velocity. "C" and "X" represent the linear viscous case $m = 1$ and the more plastic $m = 5$ case respectively, and the red and blue lines represent the grounding lines in respective cases.

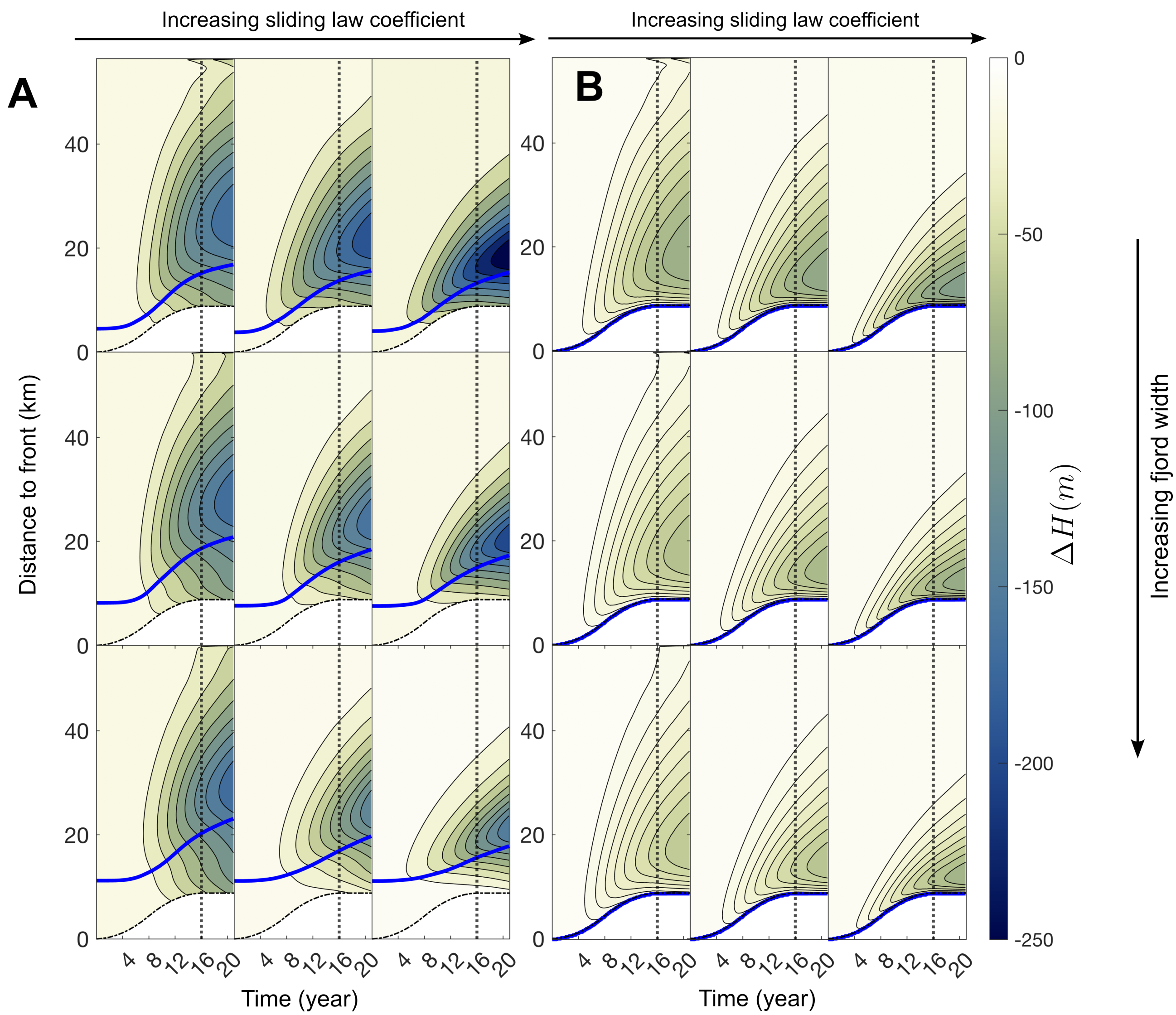

Fig. A4. Dynamic thickness change at **deep** and **shallow** testbed glaciers attributed to overburden pressure change in the sliding law, using $m = 1$. Blue lines represent the grounding lines. A) deep testbed glaciers. B) shallow testbed glaciers.

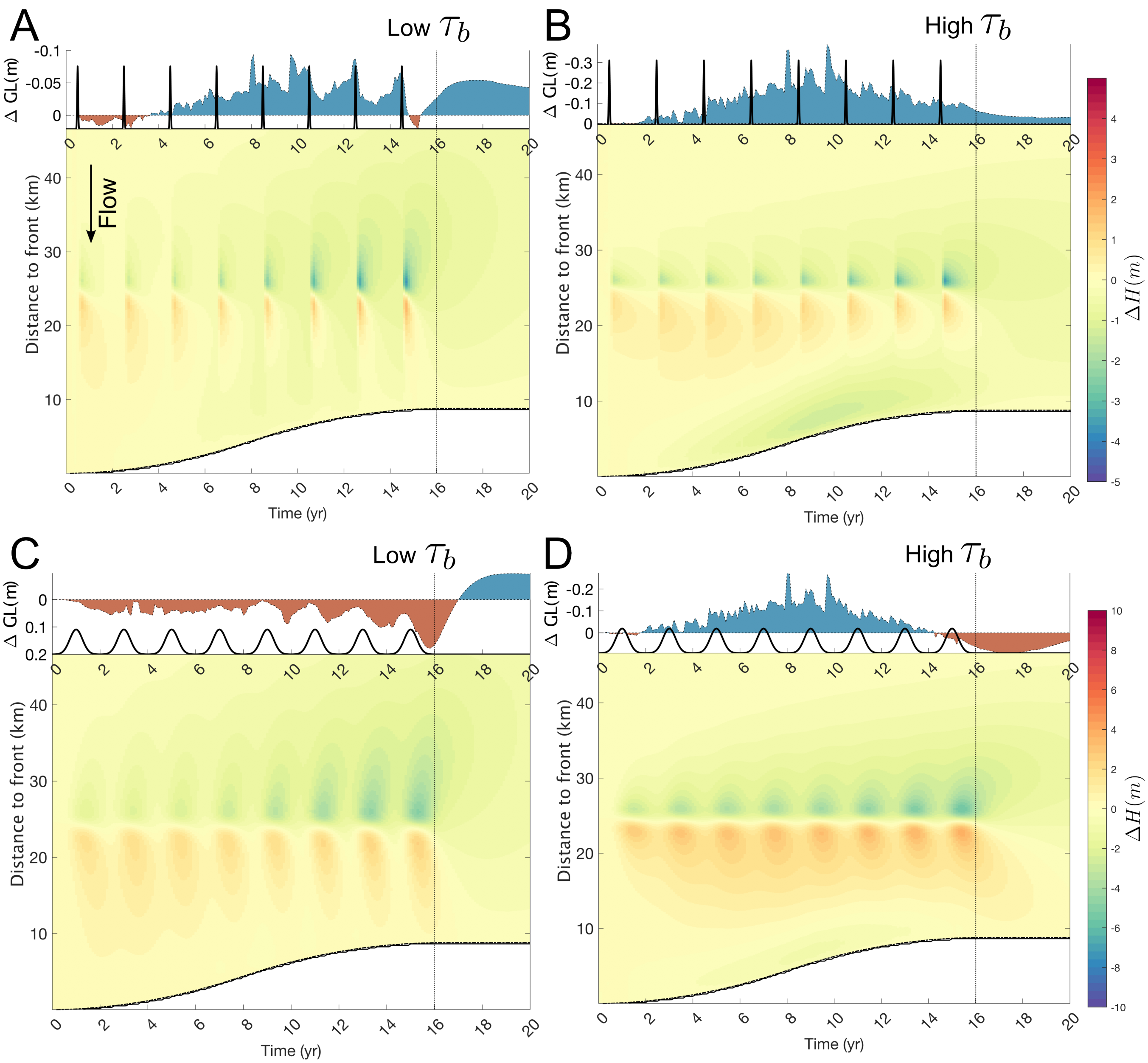

Fig. A5. Spatio-temporal pattern of dynamic thickness change along the center flow line at **narrow** and **shallow** testbed glaciers in response to the two types of localized basal perturbation pulses. All testbed glaciers remain almost fully grounded and hence the fronts and grounding lines overlap on the plots. Graphic features and subplot arrangements are the same as Fig. 4.

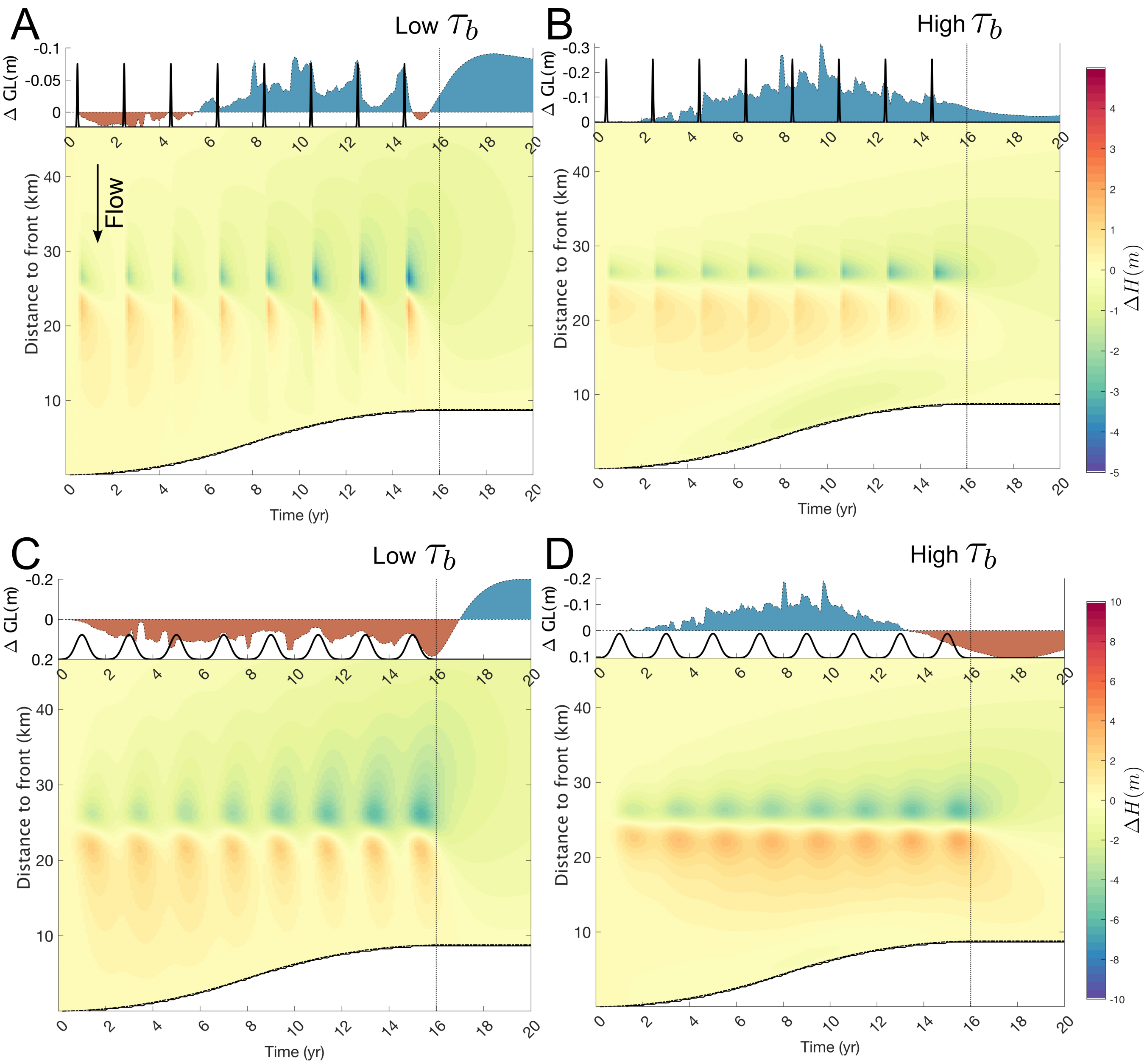

Fig. A6. Spatio-temporal pattern of dynamic thickness change along the center flow line at **wide** and **shallow** testbed glaciers in response to the two types of localized basal perturbation pulses. All testbed glaciers remain almost fully grounded and hence the fronts and grounding lines overlap on the plots. Graphic features and subplot arrangements are the same as Fig. 5.

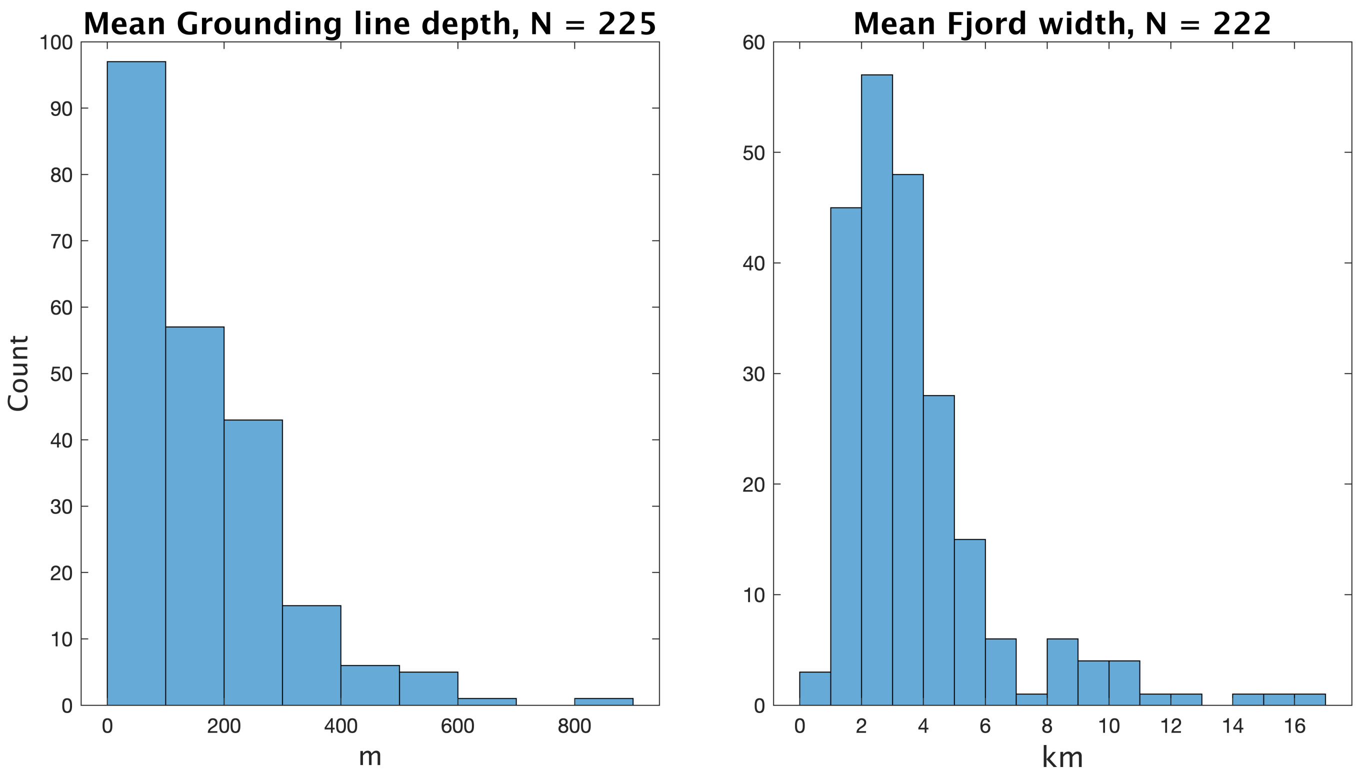

Fig. A7. Distributions of mean fjord width and grounding line depth in observational data around most of the Greenland outlet glaciers, plotted from Wood and others (2021). N is the total number of available glacier data in the original study.